The Astrophysical Journal Letters, 797:L13 (5pp), 2014 December 20 doi:10.1088/2041-8205/797/2/L13

FERMI-LAT DETECTION OF PULSED GAMMA-RAYS ABOVE 50 GeV FROM THE VELA PULSAR

Gene C. K. Leung[1], J. Takata[1], C. W. Ng[1], A. K. H. Kong[2], P. H. T. Tam[2], C. Y. Hui[3], and K. S. Cheng[1]
[1] Department of Physics, The University of Hong Kong, Pokfulam Road, Hong Kong; gene930@connect.hku.hk, takata@hku.hk
[2] Institute of Astronomy and Department of Physics, National Tsing Hua University, Hsinchu, Taiwan
[3] Department of Astronomy and Space Science, Chungnam National University, Daejeon, Korea
Received 2014 August 26; accepted 2014 October 19; published 2014 December 1

ABSTRACT

The first *Fermi*-Large Area Telescope (LAT) catalog of sources above 10 GeV reported evidence of pulsed emission above 25 GeV from 12 pulsars, including the Vela pulsar, which showed evidence of pulsation at >37 GeV energy bands. Using 62 months of *Fermi*-LAT data, we analyzed the gamma-ray emission from the Vela pulsar and searched for pulsed emission above 50 GeV. Having confirmed the significance of the pulsation in 30–50 GeV with the *H* test (*p*-value $\sim 10^{-77}$), we extracted its pulse profile using the Bayesian block algorithm and compared it with the distribution of the five observed photons above 50 GeV using the likelihood ratio test. Pulsation was significantly detected for photons above 50 GeV with a *p*-value of $= 3 \times 10^{-5}$ (4.2σ). The detection of pulsation is significant above 4σ at >79 GeV and above 3σ at >90 GeV energy bands, making this the highest energy pulsation significantly detected by the LAT. We explore the non-stationary outer gap scenario of the very high-energy emissions from the Vela pulsar.

Key words: gamma rays: stars – pulsars: individual (PSR J0835−4510) – radiation mechanisms: non-thermal

Online-only material: color figures

1. INTRODUCTION

The mechanism of the GeV gamma-ray emissions from pulsars remains to be solved since the discovery of gamma-ray emitting pulsars (Crab and Vela) in the 1970s. In the past several years, the observations of pulsar emissions above 10 GeV by the *Fermi*-Large Area Telescope (*Fermi*-LAT) and ground-based Cherenkov telescopes have created a breakthrough in the understanding of the nature of GeV gamma-ray emissions from the Crab pulsar. In particular, the detection of the pulsed emission up to 400 GeV by the MAGIC collaboration (Aliu et al. 2008; Aleksic et al. 2014) and the VERITAS Collaboration et al. (2011) were unexpected by the standard curvature radiation scenario of the outer magnetospheric gap. The observed spectrum between 100 MeV and 400 GeV is better described by a broken power law than the power law with exponential cutoff in the standard curvature radiation scenario. This result suggests that the inverse-Compton scattering process produces emissions above 10 GeV in the Crab pulsar (Aleksic et al. 2011; Aharonian et al. 2012).

In the first *Fermi*-LAT catalog of sources above 10 GeV (1FHL, Ackermann et al. 2013), 20 pulsars were found to show pulsed emissions (*p*-value $\leqslant 0.05$) in the energy range >10 GeV, including 12 pulsars showing pulsed emissions at >25 GeV (Saz Parkinson et al. 2012). 1FHL also reported evidence of pulsation from the Vela pulsar at >37 GeV and two other pulsars (PSRs J0614−3329 and J1954+2836) at >60 GeV. Recently, pulsed emission of the Vela pulsar above 30 GeV was also reported by the H.E.S.S. collaboration (2014), with a mean photon energy of 40 GeV.

Given the high significance detection of the Vela pulsar in 1FHL (e.g., $TS = 72$ in 30–100 GeV), it is a good candidate for studying pulsed emission at high energy. The recent release of the reprocessed Pass 7 (P7REP) LAT data provides significant improvement over Pass 7 (P7) in the direction reconstruction of high-energy photons >3 GeV as well as improvement in energy reconstruction (Bregeon et al. 2013). For instance, the 95% (68%) containment angle for "Source" class events at ∼50 GeV is reduced by ∼40% from 0.°8 (0.°2) in P7 to 0.°5 (0.°12) in P7REP. The reduced point-spread function at high energy implies that the number of background photons, primarily from Vela-X in this case, inside the 95% containment angle of the target source is also reduced, leading to an enhanced signal-to-noise at high energy.

In this paper, we report on the analysis of 62 months of *Fermi*-LAT data and the high significance (4.2σ) detection of pulsed emissions at >50 GeV from the Vela pulsar. The detection of pulsation is significant above 4σ at >79 GeV and above 3σ at >90 GeV energy bands.

2. OBSERVATIONS AND DATA ANALYSIS

In this study, we analyzed *Fermi*-LAT data collected for 62 months, from 2008 August 4 to 2013 October 18. The data was reduced and analyzed using the *Fermi* Science Tools package (v9r32p5), available from the *Fermi* Science Support Center.[4] We selected only events in the reprocessed Pass 7 "Source" class and used the P7REP_SOURCE_V15 IRFs. To reduce contamination from the Earth's albedo, we excluded time intervals when the zenith angle of the ROI was greater than 100° or the LAT's rocking angle was greater than 52°. We calculated the pulse phases using the `TEMPO2` plugin for *Fermi*, with the timing model of the Vela pulsar available from *Fermi*-LAT Multiwavelength Coordinating Group[5] (Ray et al. 2011), which covers the entire span of the observation.

2.1. Spectral Analysis

We performed binned likelihood analyses using the `gtlike` tool in the region surrounding the Vela pulsar. We selected photons between 0.1 and 300 GeV within a 20° × 20° ROI centered at the position of the Vela pulsar. We modeled the diffuse backgrounds with gll_iem_v05_rev1.fit and iso_source_v05.txt. We

[4] http://fermi.gsfc.nasa.gov/ssc/data/analysis/software/
[5] https://confluence.slac.stanford.edu/display/GLAMCOG/LAT+Gamma-ray+Pulsar+Timing+Models

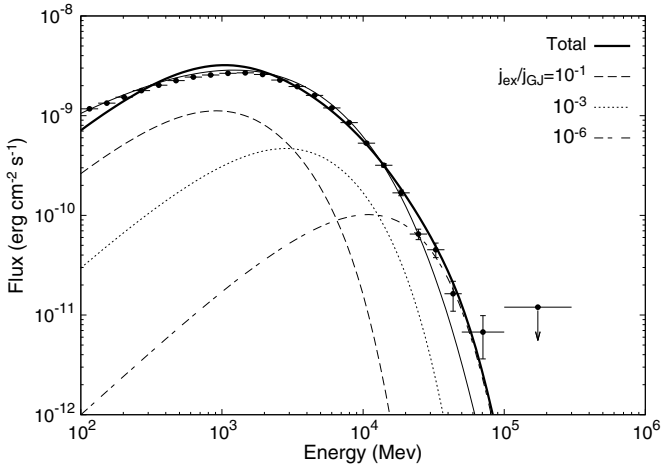

Figure 1. Phase-averaged gamma-ray spectrum of the Vela pulsar. The thick solid line shows the spectrum superposed on the emissions from the outer gap structures with the different injection currents. The result is for power index $p = 0.6$ as the distribution of the external current (Equation (3)). The dashed, dotted, and dashed-dotted lines show individual contribution of the outer gap with $j_{ex}/j_{GJ} = 10^{-1}$, 10^{-3}, and 10^{-6}, respectively. We assume the inclination angle $\alpha = 65°$. The thin solid line shows the observational fit described by Equation (1).

included 2FGL sources (Nolan et al. 2012) within 15° of the ROI center in the model. Only the spectral parameters of sources within 8° of the ROI center were left free, while others were fixed to the catalog values. Since the publication of 2FGL, extended emission from two nearby supernova remnants, Vela-Jr (Tanaka et al. 2011) and Puppis A (Hewitt et al. 2012), have been reported. The spatial and spectral models of the PWN Vela-X was also updated (Grondin et al. 2013). To model these extended sources, we first performed an off-pulse analysis for the region. We selected photons in the phase interval 0.8–1.0 (see Figure 3) for the off-pulse analysis as in Grondin et al. (2013).

We replaced the seven point sources in 2FGL that were possibly associated to Vela-Jr and Puppis A (Nolan et al. 2012) with the best-fit uniform circular disk spatial templates and simple power laws reported in Tanaka et al. (2011) and Hewitt et al. (2012). For Vela-X, we replaced the uniform circular disk model in 2FGL with the best-fit uniform elliptical disk template and broken power law reported by Grondin et al. (2013). Only the flux normalization parameters were left free. The off-pulse analysis was done with the Vela pulsar removed.

The off-pulse fit results, after correcting for exposure difference, were then passed to a phase-averaged fit. The fluxes of the three extended sources were fixed to the exposure-corrected off-pulse values. The Vela pulsar was modeled with a power law with exponential cutoff

$$\frac{dN}{dE} = N_0 \left(\frac{E}{E_0}\right)^{-\Gamma} \exp\left[-\left(\frac{E}{E_{\rm cut}}\right)^{b}\right]. \quad (1)$$

The best-fit values for the phase-averaged spectrum are $\Gamma = 1.086 \pm 0.004$, $E_{\rm cut} = 383 \pm 5$ MeV, and $b = 0.510 \pm 0.002$. The best fit function is overplotted in Figure 1.

Spectral points were obtained by performing likelihood fits in individual energy bands, fitting only the normalization parameters of the Vela pulsar and point sources within 4°, modeled as power laws, and the diffuse backgrounds. All other sources were fixed to the best-fit full band values. For the energy bands 50–100 GeV and 100–300 GeV, the normalization parameter of Vela-X was also left free. The

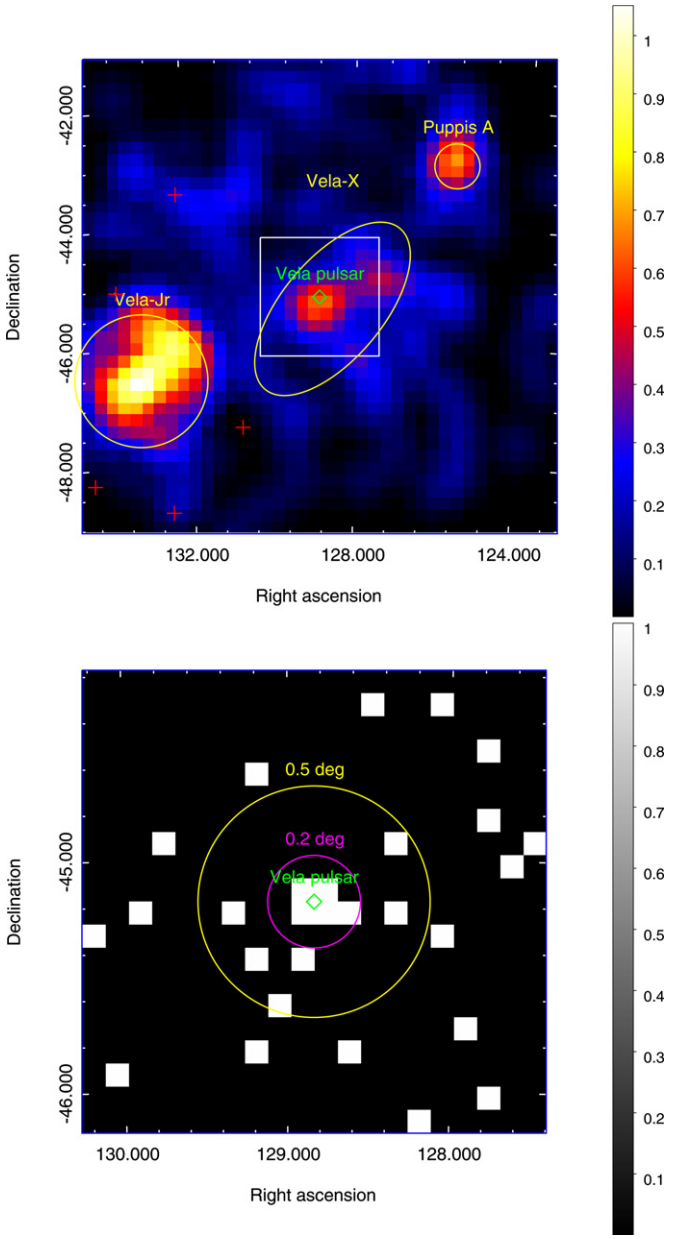

Figure 2. Upper panel: smoothed counts map of the 8° × 8° region with 0.°2 × 0.°2 pixel size. The Vela pulsar is labeled with a green diamond, 2FGL sources with red crosses, and extended sources with yellow ellipses. The white square represents the region shown in the lower panel. Lower panel: counts map of the 2° × 2° region with 0.°1 × 0.°1 pixel size. No smoothing is applied. The five photons with $P_{\rm PSR} > \max(P_{\rm PWN}, P_{\rm GAL})$ are all located within the 0.°2 radius circle.

(A color version of this figure is available in the online journal.)

results are shown in Figure 1. The Vela pulsar is detected in 50–100 GeV with a TS value of 9.5 (3.1σ) and a photon flux of $(3.17 \pm 1.78) \times 10^{-11}$ photons cm^{-2} s^{-1}. In 100–300 GeV, the TS value of the Vela pulsar drops to 2.4 (1.5σ) and the 95% c.l. upper limit was shown.

A spectral fit was performed in 50–300 GeV. The source model was the same as above, except that the Vela pulsar and Vela-X were now modeled as power laws with the normalization factors and spectral indices left free. The Vela pulsar was detected with a TS value of 11.7 (3σ), with a photon index of -2.53 ± 0.98 and a photon flux of $(4.27 \pm 2.13) \times 10^{-11}$ ph cm^{-2} s^{-1}. Figure 2 (upper panel) shows the smoothed

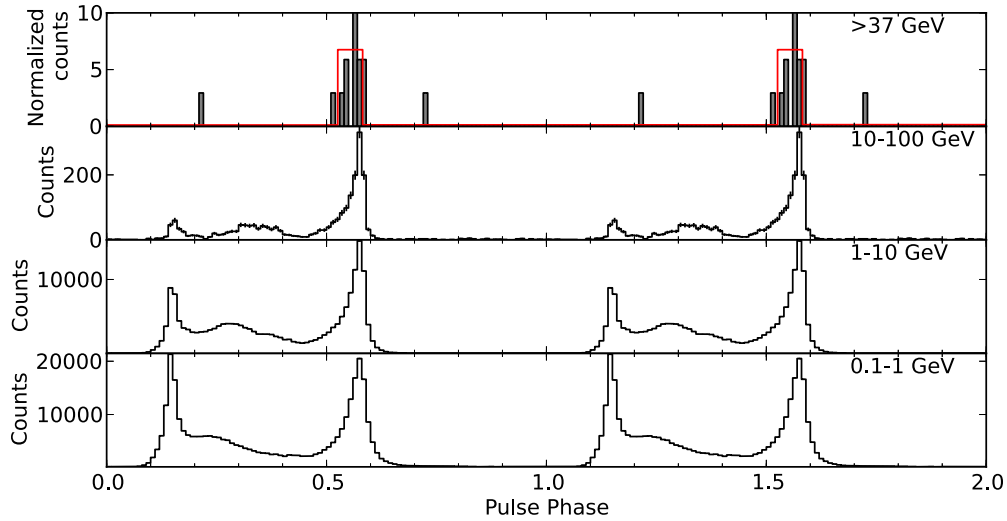

Figure 3. (a) Weighted light curve in 50–300 GeV. (b) Folded light curve in 30–50 GeV with a 0.°4 radius aperture. The black histogram represents the observed counts and the red line represents the Bayesian block decomposition. Folded light curves in (c) 10–100 GeV, (d) 1–10 GeV, and (e) 0.1–1 GeV with a 1° radius aperture. (A color version of this figure is available in the online journal.)

counts map above 50 GeV in a 8° × 8° region. The emission around the position of the Vela pulsar is point-like and distinct from that of Vela-X. In contrast, the emission from Vela-Jr, with a spatial template of comparable size, is visibly extended.

2.2. Pulsation Search

2.2.1. Weighted H Test

Given the significant detection of the Vela pulsar in 50–300 GeV, we performed a pulsation search in this energy range. We applied a weighted H test (Kerr et al. 2011) to this energy range. Each photon within 4° from the Vela pulsar was weighted by its probability of having originated from the pulsar ($P_{\rm PSR}$), calculated using the `gtsrcprob` tool. We used the spectral model obtained from the spectral fit in 50–300 GeV described in Section 2.1 to calculate the probabilities. The sum of probabilities $\sum P_{\rm PSR} = 6.3$ and the weighted H statistic is 15.4, corresponding to a p-value of 0.002 or 3.1σ. Figure 3(a) shows the weighted light curve in 50–300 GeV. The weighted H test for higher energy ranges returned $H < 15$, i.e., below 3σ.

As noted in 1FHL, the H test (de Jager et al. 1989; Kerr et al. 2011) is not the most sensitive tool for the pulsation search on known pulsars at high energy, as it does not utilize any prior knowledge of the pulse shape. Therefore, we apply a likelihood ratio test in our search. The test compares the distribution in pulse phase of high-energy photons with a known pulse profile in lower energies, and determines whether the high-energy photons are better described by the known pulse profile or a uniform distribution. For this test to be most effective, it is necessary that the lower-energy pulse profile should satisfactorily reflect the expected distribution of high-energy photons.

2.2.2. Selection of Low-energy Pulse Profile

As shown in previous studies (e.g., Abdo et al. 2010, 2013), the pulse profile of the Vela pulsar is strongly dependent on energy. Figure 3(c) to (e) shows the folded light curves of the Vela pulsar in three energy bands: 0.1–1 GeV, 1–10 GeV, and 10–100 GeV. With increasing energy, P1 weakens significantly, with the peak heights ratio P1:P2 decreasing by a factor of ∼5 from 0.1–1 GeV to 10–100 GeV. The bridge structure also shifts toward P2 and reduces in height. Therefore, it is expected that the photons above 50 GeV should follow a distribution more similar to that in 10–100 GeV and concentrate around P2, and it is not appropriate to apply the full energy pulse profile in the likelihood ratio test.

In order to obtain a pulse profile that better reflects the high-energy behavior, we need to use an energy range high enough to reflect the expected distribution of the >50 GeV photons, but low enough to demonstrate a statistically significant pulse profile. We extracted the folded light curve in 30–50 GeV and performed the unweighted H test (de Jager et al. 1989). We experimented with different aperture radii in steps of 0.°1 and found that a 0.°4 radius maximizes the H statistic, giving $H = 440$ (p-value $\sim 10^{-77}$). This represents a statistically significant pulse profile to be used in the likelihood ratio test.

We then employed the Bayesian block algorithm (Scargle et al. 2013) to identify statistically significant variation features in the folded light curve in 30–50 GeV in a 0.°4 radius aperture, using a false positive threshold of 0.5%. Since the Bayesian block algorithm assumes Poisson statistics, it can only be applied to unweighted photons. The folded light curve in 30–50 GeV is represented by a block spanning the phase interval from 0.5159 to 0.5870. Figure 3(b) shows the 30–50 GeV folded light curve overlaid with the Bayesian blocks. This block function was taken to be the low-energy pulse profile in the likelihood ratio test.

2.2.3. Photon Selection Above 50 GeV

To select >50 GeV photons for the likelihood ratio test, we also calculated the probabilities of coming from Vela-X ($P_{\rm PWN}$) and the Galactic diffuse emission ($P_{\rm GAL}$) for photons within 4° from the Vela pulsar, following the procedures described in Section 2.2.1. Since the Vela pulsar is completely embedded in Vela-X as seen by the LAT, the major sources of background contamination are Vela-X and the Galactic diffuse emission. Therefore, we selected only photons with $P_{\rm PSR} > \max(P_{\rm PWN}, P_{\rm GAL})$.

A total of five photons have $P_{\rm PSR} > \max(P_{\rm PWN}, P_{\rm GAL})$. Figure 2 (lower panel) displays the counts map above 50 GeV. All the five photons are located within the 0.°2 circle centered at the Vela pulsar. We also note that all five photons fall into the highest quality "Ultraclean" class of events, meaning that they

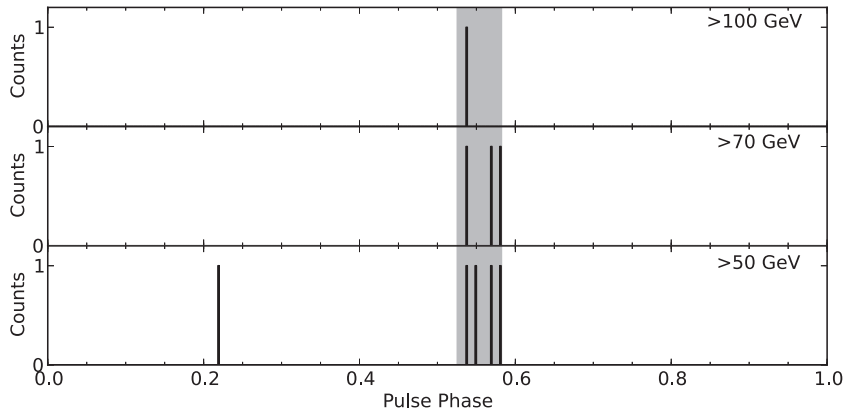

Figure 4. Folded light curves for 50–300 GeV (bottom), 70–300 GeV (middle), and 100–300 GeV (top). The shaded area represents the on-peak interval decided by Bayesian blocks at 30–50 GeV.

Table 1
Energy, Arrival Time, Angular Separation from the Vela Pulsar, Pulse Phase, and Source Probability of >50 GeV Photons with $P_{\rm PSR} > \max(P_{\rm PWN}, P_{\rm GAL})$ in Ascending Order of Energy

E_γ (GeV)	Time (MJD)	$\Delta\theta$ (°)	Pulse Phase	$P_{\rm PSR}$	$D_{E\geqslant E_\gamma}$	$p_{E\geqslant E_\gamma}$	$\sigma_{E\geqslant E_\gamma}$
51.3	55050.8	0.074	0.548	0.940	16.3	3.3×10^{-5}	4.2σ
55.9	56149.3	0.136	0.219	0.707	11.5	4.2×10^{-4}	3.5σ
79.5	56317.2	0.034	0.581	0.986	15.9	6.0×10^{-5}	4.0σ
91.0	56437.5	0.011	0.569	0.994	10.6	1.4×10^{-3}	3.3σ
208.5	55154.1	0.092	0.537	0.922	5.3	2.8×10^{-2}	2.2σ

Notes. Three glitches occurred at MJD 53959.9, MJD 55408.8, and MJD 56555.8. The D value, p-value, and significance of pulsation at the energy range bounded below by E_γ of each photon are also shown.

have the strictest rejection against cosmic ray events, which are more common at higher energies. Figure 4 shows the folded light curves in three energy bands: 50–300 GeV, 70–300 GeV, and 100–300 GeV. The shaded area represents the phase interval spanned by the Bayesian block in 30–50 GeV. Four of the five photons are located within the Bayesian block and are distributed across all three energy bands. The highest energy photon within the Bayesian block is at 209 GeV. Table 1 lists the energy, arrival time, angular separation from the Vela pulsar, pulse phase, and source probability of the five photons. We note that one glitch occurred at MJD 53959.9 (Yu et al. 2013) before the start of the observation, and two other glitches were recorded during the span of the observation at MJD 55408.8 and MJD 56555.8 in the timing model. None of the selected photons was detected near a glitch epoch.

2.2.4. Likelihood Ratio Test

We performed a maximum likelihood fit to the >50 GeV folded light curve using a probability distribution of a block function

$$\mathrm{PDF}(\phi) = \begin{cases} 1 - s + \frac{s}{\phi_1 - \phi_0} & \text{if } \phi_0 \leqslant \phi \leqslant \phi_1 \\ 1 - s & \text{otherwise,} \end{cases} \quad (2)$$

where ϕ is the pulse phase, ϕ_0 and ϕ_1 are fixed to the edges of the Bayesian block in 30–50 GeV, and s is a free parameter in [0, 1]. We also performed a fit with the null hypothesis of a uniform distribution, i.e., $s = 0$. Using the likelihood ratio test, we obtained the test statistic, $D = -2\Delta\log(\text{Likelihood}) = 16.3$ for $E > 50$ GeV. We scanned up in energy by removing the lowest-energy photon each time and calculating the D value. The D values are listed in Table 1.

Since the Wilk's theorem, which translates D to p-values, assumes infinite statistics, we calculated the p-values with Monte Carlo simulations. In each Monte Carlo realization, N phases, where N is drawn from a Poisson distribution with the mean equal to the observed number of photons, were randomly generated in [0, 1]. Then the same analysis was performed to the simulated data to calculate the D value. The p-values from Monte Carlo simulation agree with Wilk's theorem and are listed in Table 1. The significance of pulsation is above 4σ for >51 and >79 GeV, and above 3σ at >90 GeV energy bands. We note that the pulsation significance for >55 GeV is below 4σ, due to the contribution of an off-pulse photon at 55.9 GeV. We also note that, however, this particular photon has a smaller probability (∼0.7) to have originated from the Vela pulsar than the other four photons (>0.9).

3. DISCUSSION

As shown in Figure 1, the observed flux above 10 GeV of the Vela pulsar decreases slower than a simple exponential function. Previous emission models that invoke the curvature radiation process for the GeV emissions have in general predicted a flux at the 50–100 GeV smaller than the observed flux level of 10^{-12} erg cm^{-2} s^{-1}. Abdo et al. (2010) proposed that a subexponential cutoff in the observed spectrum can be understood as the superposition of several power low plus exponential cutoff functions with varying the photon index and the cutoff energy.

In the section, we argue the model that the outer gap accelerator is switching between a number of states, and that superposition of the emissions from the different states of the outer gap make the observed spectrum of *Fermi*. There is a wide range of variability times scale in the radio emissions from the pulsar (e.g., Kramer et al. 2002; Lyne et al. 2010; Keane 2013). The

micro-second variations seen in single pulse could be produced by spatial fluctuation in the emission region. The pulse-to-pulse variations on the timescale of milliseconds to seconds likely represent the timescale of the temporal variation of the structure of the emission region. The longer timescale (seconds to years) variations associated with the model switching and nulling, which sometimes accompany the variations of the spin down rate, could be related with the changes of entire magnetosphere. The higher-energy observations also found the mode switches in the X-ray emission properties of PSR B0943+10 (Hermsen et al. 2013) and in the GeV gamma-ray emission properties of PSR J2021+4026 (Allafort et al. 2013). These multi-wavelength observations suggest that the switching between a number of state of magnetosphere is probably a generic feature of the pulsars.

The active outer gap should require the external currents ($j_{\rm ex}$) that are injected into the outer gap at the boundaries because they initiate the gamma-ray emissions and subsequent pair-creation cascade process. In our model, the outer gap structure and the properties of the curvature radiation depend on how large currents are injected into the gap. For example, the outer gap size can develop until the pair-creation process creates the gap current of the order of the Goldreich–Julian value $j_{\rm GJ} \sim \Omega B/2\pi$ (Takata et al. 2004; Hirotani 2006). The outer gap with a smaller external current has a larger gap size and a larger electric field, and produces harder gamma-rays. If the external current, which may be originated from the polar cap region, is temporally variable, the observed gamma-ray spectrum will be the superposition of the emissions from various gap states.

We consider that the outer gap (Cheng et al. 1986; Takata et al. 2006) produces the GeV emissions; in the model the charge depletion from the Goldreich–Julian charge density causes the electric field along the magnetic field line, which accelerates the electrons and positrons to Lorentz factor of $\sim 10^7$. We assume the dipole magnetic field in the magnetosphere and solve three-dimensional (3D) structure of the gap (J. Takata et al. in preparation); (1) the particle acceleration process by the electric field, (2) the curvature radiation process, and (3) the pair-creation process between the gamma-rays and thermal X-rays from the neutron star surface. Our 3D model is the expansion of a two-dimensional study developed by Takata et al. (2006, 2008) and Takata & Chang (2009), which discussed the phase-averaged spectra of the pulsars measured by the EGRET.

In our model, we assume that the observed gamma-ray spectrum is a superposition of the emissions from various *stationary* gap structures with various external currents. The model assumes that the timescale of the variability of the external current is of the order of or longer than the crossing timescale of the light cylinder radius (r_{lc}), $\tau \sim r_{lc}/c = p/2\pi$, with which the stationary outer gap structure for an external current is archived. Figure 1 compares the calculated spectra with the observations. In the calcualtion, we assumed the power-law distribution of the external current as

$$I = K j_{\rm ex}^{p},\ j_{\rm min} < j_{\rm ex} < j_{\rm max}, \quad (3)$$

where K is the normalization factor and is determined from $\int (dI/dj_{\rm ex}) dj_{\rm ex} = 1$, and we used $j_{\rm min} = 10^{-6} j_{\rm GJ}$ and $j_{\rm max} = 0.2\, j_{\rm GJ}$. In addition, we chose the power index $p \sim 0.6$, which reasonably reproduces the observed spectral cutoff behavior. In Figure 1, the calculated spectrum for *an external current* cannot explain the observed spectral shape in 100 MeV–50 GeV, while the gamma-ray spectrum superposed by the different gap states better explains the observed cutoff behavior. We also find that the emissions above 20 GeV can be explained by the outer gap with a very small injection current. In a subsequent paper, we will study dependency of the viewing geometry (inclination angle and viewing angle) on the predicted spectrum and will discuss the goodness of the model fitting for high-energy pulsars.

In summary, we detected pulsed gamma-ray emissions from the Vela pulsar at above 4σ at >79 GeV and above 3σ at >90 GeV energy bands using *Fermi*-LAT. This is difficult to explain using the previous stationary model in the pulsar magnetosphere. We proposed the model that the outer gap structure switches between a number of state. Future searches for pulsed emission above 50 GeV in other pulsars will help us to understand the nature of the high-energy emission in the pulsar magnetosphere.

We thank anonymous referee, P. M. Saz Parkinson, and J. E. McEnery for useful comments and suggestions, and E. M. H. Wu, and J. H. K. Wu for providing the weighted H-test computing code. This work is partially supported by a 2014 GRF grant under HKU 17300814P and Seed Funds under HKU 20127159004 and 201310159026. A.K.H.K. and P.H.T. are supported by the National Science Council of the Republic of China (Taiwan) through grants 100-2628-M-007-002-MY3 and 100-2923-M-007-001-MY3, and 101-2112-M-007-022-MY3, respectively. C.Y.H. is supported by a research fund from Chungnam National University in 2014. J.T. acknowledges TIARA, operated under the ASIAA of Taiwan to use their PC cluster.

REFERENCES

Abdo, A. A., Ackermann, M., Ajello, M., et al. 2010, ApJ, 713, 154
Abdo, A. A., Ajello, M., Allafort, A., et al. 2013, ApJS, 208, 17
Ackermann, M., Ajello, M., Allafort, A., et al. 2013, ApJS, 209, 34
Aharonian, F. A., Bogovalov, S. V., & Khangulyan, D. 2012, Natur, 482, 507
Aleksic, J., Alvarez, E. A., Antonelli, L. A., et al. 2011, ApJ, 742, 43
Aleksic, J., Ansoldi, S., Antonelli, L. A., et al. 2014, A&A, 565, L12
Allafort, A., Baldini, L., Ballet, J., et al. 2013, ApJL, 777, 2
Aliu, E., Anderhub, H., Antonelli, L. A., et al. 2008, Sci, 322, 1221
Bregeon, J., Charles, E., & Wood, M. 2013, arXiv:1304.5456
Cheng, K. S., Ho, C., & Ruderman, M. 1986, ApJ, 300, 500
de Jager, O. C., Raubenheimer, B. C., & Swanepoel, J. W. H. 1989, A&A, 221, 180
Grondin, M.-H., Romani, R. W., Lemoine-Goumard, M., et al. 2013, ApJ, 744, 110
Hermsen, W., Hessels, J. W. T., Kuiper, L., et al. 2013, Sci, 339, 436
H.E.S.S. Collaboration. 2014, in Astroparticle Physics 2014: A Joint TeVPA/iDM Conference, https://www.mpi-hd.mpg.de/hfm/HESS/201406-TeVPA-Amsterdam-nofilm.pdf
Hewitt, J. W., Grondin, M.-H., Lemoine-Goumard, M., et al. 2012, ApJ, 759, 89
Hirotani, K. 2006, ApJ, 652, 1475
Keane, E. F. 2013, in IAU Symp. 291, Neutron Stars and Pulsars: Challenges and Opportunities after 80 Years, ed. J. van Leeuwen (Cambridge: Cambridge Univ. Press), 295
Kerr, M. 2011, ApJ, 732, 38
Kramer, M., Johnston, S., & Van Straten, W. 2002, MNRAS, 334, 523
Lyne, A., Hobbs, G., Kramer, M., Stairs, I., & Stappers, B. 2010, Sci, 329, 408
Nolan, P. L., Abdo, A. A., Ackermann, M., et al. 2012, ApJS, 199, 31
Ray, P. S., Kerr, M., Parent, D., et al. 2011, ApJS, 194, 17
Saz Parkinson, P. M., et al. 2012, in Proc. AIP Conf. 1505, High Energy Gamma-Ray Astronomy, ed. F. A. Aharonian, W. Hofmann, & F. M. Rieger (Melville, NY: AIP), 293
Scargle, J. D., Norris, J. P., Jackson, B., & Chiang, J. 2013, ApJ, 764, 167
Takata, J., & Chang, H.-K. 2009, MNRAS, 392, 400
Takata, J., Chang, H.-K., & Shibata, S. 2008, MNRAS, 386, 748
Takata, J., Shibata, S., & Hirotani, K. 2004, MNRAS, 354, 1120
Takata, J., Shibata, S., Hirotani, K., & Chang, H.-K. 2006, MNRAS, 366, 1310
Tanaka, T., Allafort, A., Ballet, J., et al. 2011, ApJL, 740, L51
VERITAS Collaboration., et al. 2011, Sci, 334, 69
Yu, M., Manchester, R. N., Hobbs, G., et al. 2013, MNRAS, 429, 688